



Characterization of stress perturbations near major fault zones: insights from 2-D distinct-element numerical modelling and field studies (Jura mountains)

C. HOMBERG, J. C. HU, J. ANGELIER, F. BERGERAT and O. LACOMBE

Université P. et M. Curie, URA 1759, CNRS, Laboratoire de Tectonique Quantitative, Tr 25-26, E1,
Boîte 129, 4 place Jussieu, 75252 Paris, Cedex 05, France

(Received 9 April 1996; accepted in revised form 19 November 1996)

Abstract—We consider and discuss the presence of discontinuities in the crust as a major source of stress perturbations. Based on 2-D distinct-element modelling, we reconstruct the local stress field around a vertical discontinuity in various geological contexts. The resulting stress distribution reveals that major directional stress changes occur near the tips of the discontinuity so that stress deviations can reach values as large as 50°. We establish simple relationships controlling stress changes around a pre-existing fault zone as a function of (1) the remote differential stress magnitude, ($\sigma_1 - \sigma_3$), (2) the friction coefficient on the discontinuity, and (3) the strike of the discontinuity relative to the far-field stress.

As a geological example, we present the Morez Fault Zone in the internal Jura. Paleostress reconstruction in forty-two sites indicates that the trends of the Mio-Pliocene compression are N110° on average near the fault, whereas they are N130° in the surrounding areas. A comparison between the results of the tectonic study and those of theoretical modelling suggests that the 20° counterclockwise deviation is directly related to the reactivation of this large weak zone. We thus evaluate the role of mechanical decoupling along pre-existing zones of weakness, especially with consideration to the accommodation of the Alpine deformation in the Jura belt. © 1997 Elsevier Science Ltd.

INTRODUCTION

Tectonic studies often show that discontinuous deformation plays a major role in the evolution of large regions such as mountain belts. For instance, where compressional tectonism occurs, most of the deformation takes place in thrust zones (or in zones of intensive folding). This inhomogeneous aspect of the deformation is illustrated in the external Jura; most of the outer Jura belt consists of plateaus, separated by narrow zones where the Neogene Alpine deformation is concentrated by both fracturing and folding modes (Caire, 1960). In terms of stress fields, the stress trends and even the tectonic regime reconstructed in the vicinity of such areas where deformation has been concentrated may differ from those reconstructed in surrounding areas. One can thus distinguish, for a single tectonic episode, a local stress state characteristic of a particular folded or faulted zone, and a more widespread stress state (the far-field stress) which dominated in the surrounding regions and should be considered as representative of the regional tectonic evolution.

Numerous regional studies (e.g. De Charpal *et al.*, 1974; Mattauer and Mercier, 1980; Rispoli, 1981; Trémolières, 1981; Zoback *et al.*, 1987; Rawnsley *et al.*, 1992; Rebaï *et al.*, 1992; Arthaud and Laurent, 1995) have shown evidence for the relation between stress perturbations at different scales and the presence of pre-existing discontinuities. For instance, at the regional scale, in the Alicante region of Spain, the inhomogeneity in Miocene compressional trends has been related to the presence of dextral strike-slip faults (De Ruig, 1990). Likewise, Lacombe *et al.* (1993) interpret the 40° rotation

of the direction of Oligocene extension in the transform zone connecting the Rhine and Bresse grabens of the West European Rift system as a major regional perturbation due to sinistral slip along a pre-existing basement fault zone. Significant paleostress deviations were also documented at the outcrop scale by Petit and Mattauer (1995). According to these authors, the observed stress changes are related to the presence of, and displacement on, a strike-slip fault, and they are principally observed near fault tips.

Stress deviations, however, have not only been observed in the vicinity of fault zones, but also throughout larger areas. In the external Jura, for example, a noticeable change in the direction of extension during the Oligocene phase has been documented, with WNW–ESE trends (Homberg *et al.*, 1994), whereas it generally trends E–W in most segments of the West European Rift (Villemin, 1986; Bergerat, 1987). The major discontinuities and related mechanical decoupling within this highly fractured part of the crust between the Bresse graben and the external Jura are the most likely source of this regional deviation of stresses (Homberg, 1993).

Major discontinuities, such as fault zones inherited from older tectonic events, thus may greatly influence the accommodation of the later deformation. Because of its complex orogenic history, continental crust usually exhibits strength anisotropy caused by pre-existing fractures or zones of weakness. Discontinuities as sources of stress perturbations have previously been considered by analytical methods. These methods are based on equations of the elasticity theory and describe the distribution of different elements of the strain and stress tensors around simple fault geometries (e.g. Paris and

Sih, 1965; Jaeger and Cook, 1969; Segall and Pollard, 1987). More complex patterns of discontinuities have been analysed by means of numerical modelling (and also by a few analytical modelling experiments). These models describe the displacement field and the stress perturbations near discontinuous faults (Segall and Pollard, 1980) as well as pull-apart basins and push-up structures (e.g. Quiblier *et al.*, 1980; Xiahoan, 1983; Phan Trong, 1989). Such modelling was successful in that it allowed mechanical understanding for some typical tectonic structures, but could not result in a systematic characterization and quantification of stress perturbations (as a function of fault strikes, boundary conditions and so on). Osokina (1988) proposed an analytical resolution of this perturbation problem. He described the displacement fields along a pre-existing fault as a function of its strike, considering several different types of external stress field. Unfortunately, the stress patterns resulting from this analysis were unsufficiently described. Auzias (1995) studied, by means of analogical modelling, different geometries of pre-existing discontinuity in various biaxial compression contexts. However, geological applications have to be done carefully because the friction on the discontinuity in these models does not reflect the friction on geological faults. The friction is either under-estimated (the case of open cracks) or tightly localized (the case of contact points).

AIM OF THE STUDY

In this paper, we aim to characterize the stress perturbations induced by the presence of pre-existing discontinuities, whatever their strike and in various remote stress field contexts. To address this problem of stress perturbations around reactivated discontinuities, we use a 2-D distinct-element numerical modelling approach for its suitability to solve geological problems involving fault behaviour (see the following section on modelling). In order to exclude local complexities such as for areas where several discontinuities simultaneously induce perturbations of the stress field, we have chosen to restrict our study to simple cases where constraints are clearly defined and can be validated with geological data. We therefore consider a single discontinuity cutting into a homogeneous medium. The characterization of stress distribution near discontinuities of various strikes and in various tectonic contexts will be particularly useful for the interpretation of stress fields at a regional scale, in pre-fractured regions. First, when smoothing data from regions containing stress perturbations, it allows us to limit artificial deviation of reconstructed paleostress trajectories. This is of special importance where density of outcrops is low, and does not provide sufficient constraints for the interpolation of stress trajectories between sites. Second, it will help to interpret tectonic data in terms of regional and/or local stress states without requiring many superimposed tectonic phases.

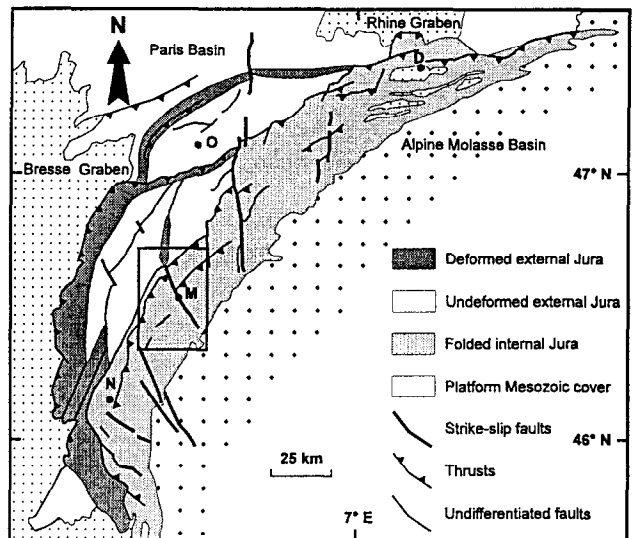


Fig. 1. Simplified structural map of the Jura and location of the area investigated (frame). D, M, N and O mark cities: Délémont, Switzerland; Morez, Nantua and Ornans, France. Modified from Chauve *et al.* (1980).

In order to check the results of modelling, a geological case study involving a relatively simple structural pattern and a good knowledge of paleostress distribution is needed. We led an extensive field study in the internal Jura (Fig. 1). Paleostress reconstruction in and around the 20 km-long Morez Fault revealed a particular distribution in the trends of the Mio-Pliocene direction of compression in the close vicinity of the fault, which underwent sinistral slip at that time (Fig. 2). Considering the aim of our study, the stress field pattern in the Morez Fault area is particularly appropriate as a geological case example, for the following reasons.

(1) Paleomagnetic studies (e.g. Gehring *et al.*, 1991) indicate that the maximum angle of block rotation in the Jura does not exceed 8° , a value which falls within the range of usual uncertainties for the stress tensor determination in brittle tectonics (see Choi, 1996 for estimates of stress tensor uncertainties). We can thus assume that for both the tectonic structures and the corresponding paleostress axes, the original orientations remained unchanged. Thus, no problem of large block rotation needs to be considered.

(2) During the Mio-Pliocene, the whole Mesozoic cover of the Jura was displaced northwestwards by about 10 km (Caire, 1960; Chauve *et al.*, 1988). It is very likely that at this time the Morez Fault already existed, and affected the whole cover (see later section on the Morez Fault). The structural pattern did not change significantly after this compressional event.

(3) The density of outcrops enables us to define in detail the paleostress states and the stress trajectory pattern through the tectonic analysis of fault slip data, thus providing tight constraints in terms of stress distribution.

(4) The stress states related to other tectonic events

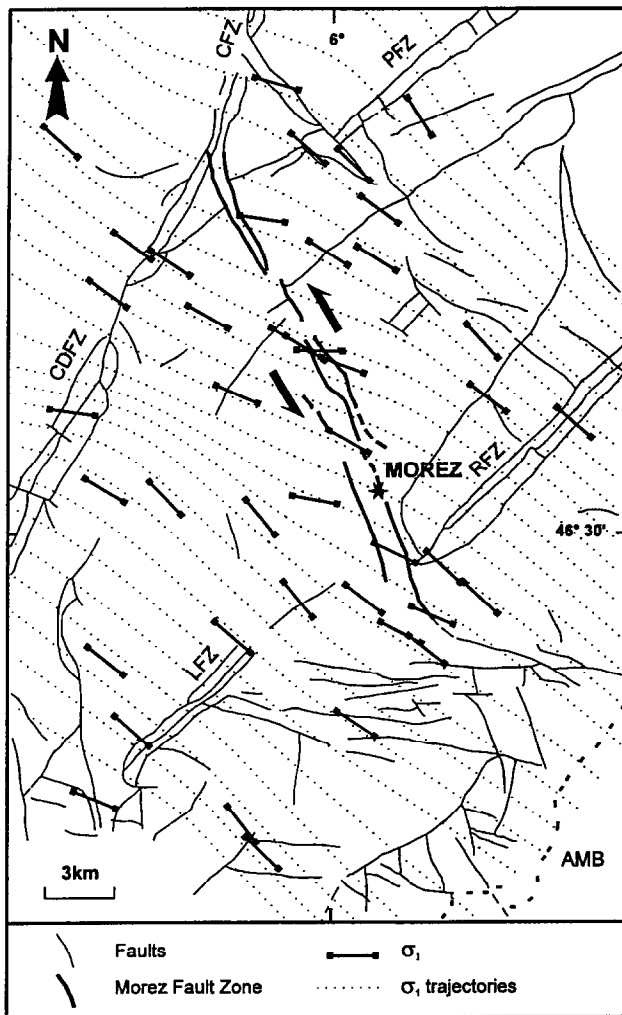


Fig. 2. Paleostress trajectories of the Mio-Pliocene compression around the Morez Fault Zone (France). The trends of σ_1 axes are obtained from fault slip inversion and the corresponding trajectories are reconstructed using the 'lissage' software (Lee and Angelier, 1994). CFZ, CDFZ, PFZ, LFZ, RFZ: thrust fault zones of Champagnole, Chaux du Dombier, Planches, Longchaumois, Rizoux (respectively). AMB: Alpine Molasse Basin.

markedly differ, in terms of direction and regime, from that of the Mio-Pliocene compression, so that no ambiguity resulting from superimposed tectonic events can confuse our results.

(5) Other discontinuities are far enough from the Morez Fault and generally trend perpendicular to the regional compressional stress of the Mio-Pliocene phase. Structural data (e.g. Guillaume and Guillaume, 1969) indicate that these discontinuities essentially underwent a vertical component of displacement during the Mio-Pliocene phase. The strike and the displacement during the Mio-Pliocene of these discontinuities differ markedly from those of the Morez Fault Zone. Thus, in the area studied, we expect that stress perturbations in the horizontal plane induced by the presence of surrounding thrust faults can be easily distinguished and may even be neglected compared to those due to the Morez Fault Zone.

(6) The paleostress states are known in the surrounding, less deformed zones of the Jura belt, such as for the plateaus of the external Jura (Tschanz, 1992; Lacombe and Angelier, 1993; Homberg *et al.*, 1994) and, at a wider scale, in the neighbouring areas of the West European Platform (Bergerat, 1987). A detailed knowledge of the regional stress state at the boundaries of the structural domain considered is thus available.

We construct a 2-D distinct-element model in order to determine whether the perturbations of the Mio-Pliocene direction of compression observed can be related to the presence of the Morez Fault Zone.

2-D DISTINCT-ELEMENT MODELLING OF STRESS DISTRIBUTION AROUND A PRE-EXISTING DISCONTINUITY

To characterize and quantify the stress perturbations around a pre-existing discontinuity, we use a 2-D distinct-element method with plane strain conditions of deformation, UDEC (Cundall, 1980). The first version of the distinct-element method was proposed by Cundall (1971) and has been continuously improved in recent years. The method has been extended to all geometries and deformabilities of blocks, new effects have been added (i.e. fluid flow in joints and block cracking) and the exploitation of the results has been facilitated with the addition of new graphics. A 2-D numerical study is an essential preliminary step to recognize the main parameters which control stress perturbations. Note that this 2-D distinct-element analysis is directly applicable to strike-slip deformations (where deformation occurs in a horizontal plane) which commonly occur in the forelands of collision belts.

The medium is divided into a finite number of blocks limited by the discontinuities included by the user and submitted to boundary conditions. In our modelling, we have used boundary stress conditions which can be expressed in terms of forces. The response to applied loading is obtained for each block by integrating Newton's second law (Eq. 1) over time at each block centroid, using the finite difference technique:

$$mx_i'' = F_i + f_i \quad i = 1, 2 \quad (1)$$

in which i represents the two reference axes, x_i'' the component in the i direction of acceleration of the block centroid, m the mass of the block, F_i the component of forces arising from any externally applied loading and f_i the component of contact forces between blocks. In other words, the time required to reach static equilibrium is divided into incremental time steps Δt , with Δt small enough to prevent propagation of information into neighbouring blocks so that the finite difference technique can be used. The total time consists of a succession of locally determined dynamic equilibrium states. For each time step, acceleration is given by Eq. (1). Using the finite

difference technique (acceleration components considered to be constant during a time step), the new velocity components (x'_i) are obtained by the integration over the time interval Δt of the acceleration:

$$x'_i(t + \Delta t/2) - x'_i(t - \Delta t/2) = \Delta t x''_i(t).$$

Using Eq. (1), the new velocity components are defined as follows:

$$x'_i(t + \Delta t/2) - x'_i(t - \Delta t/2) = \frac{\Delta t F_i(t)}{m} + \frac{\Delta t f_i(t)}{m}.$$

The same technique is used to obtain the new position for each block centroid.

Equation (1) describes the motion of rigid blocks. Because at high stress levels the deformation of the material cannot be neglected, we have chosen for our models the 'fully deformable' option for block material. This means that arbitrary deformation of blocks is permitted through discretization of each block into finite triangular zones (Fig. 3). The vertices of the triangular zones located along the discontinuities are the contact points between blocks. Equation (1) is calculated at each vertex of the triangular zones and takes the following form:

$$m x''_i = \int_s \sigma_{ij} n_j ds + F_i + f_i \quad (2)$$

where s is the surface enclosing the mass at the gridpoint, n_j is the unit normal to s , F_i and f_i are as defined above. The constitutive relation for elastic material is given in an incremental form:

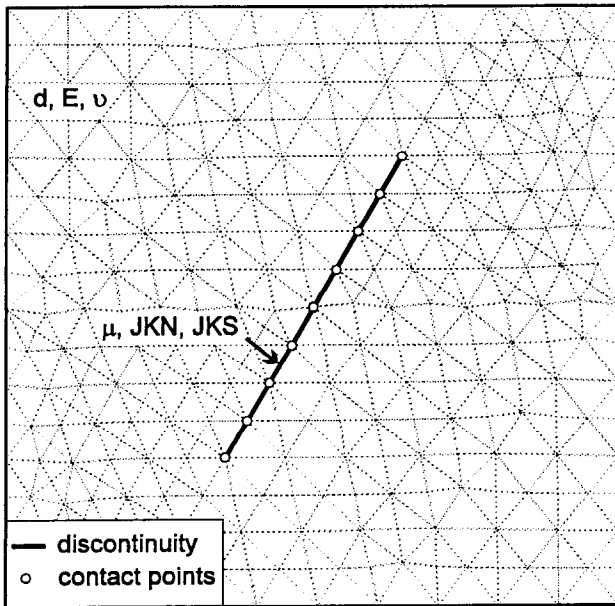


Fig. 3. Discretization of the medium into triangular zones (boundaries as dotted lines) in the distinct-element models. Mechanical properties of the elastic medium: d (density), E and ν (Young's modulus and Poisson's ratio). Mechanical properties of the discontinuity: μ (friction coefficient), JKN and JKS (normal and shear stiffnesses). Contact points along the discontinuity shown as open dots (details in the text).

$$\Delta \sigma_{ij} = \lambda \Delta \epsilon_v \delta_{ij} + 2G \Delta \epsilon_{ij} \quad (3)$$

where λ and G are the Lamé constants, $\Delta \sigma_{ij}$ and ϵ_{ij} are the stress and strain increments, $\Delta \epsilon_v = \Delta \epsilon_{11} + \Delta \epsilon_{22}$ is the increment of volumetric strain and δ_{ij} is the Kronecker function. The two elastic parameters are a function of the Young's modulus (E) and the Poisson's ratio (ν):

$$\lambda = \frac{\nu E}{(\nu + 1)(1 - 2\nu)}$$

$$G = \frac{E}{2(\nu + 1)}.$$

Equation (3) can be written as a function of E and ν , and thus becomes Eq. (4):

$$\Delta \sigma_{ij} = \frac{\nu E}{(\nu + 1)(1 - 2\nu)} \Delta \epsilon_v \delta_{ij} + \frac{E}{(\nu + 1)} \Delta \epsilon_{ij}. \quad (4)$$

During each time step, strains are related to displacement by the following relation:

$$\epsilon_{ij} = (x'_{i,j} - x'_{j,i})/2.$$

New positions of contact points between blocks (points located along the discontinuities) induce new contact forces. At contact points (Fig. 3), the force-displacement relation (Eqs 5 & 6) is defined as spring slider systems (located at each contact point) and, in our modelling, the shear stresses are limited by a Mohr-Coulomb shear failure criterion (Eq. 9). The normal and shear increments of forces (ΔF_n and ΔF_s) during one time step are thus given as follows:

$$\Delta F_n = K_n \Delta u_n \quad (5)$$

$$\Delta F_s = K_s \Delta u_s \quad (6)$$

where K_n and K_s (force per length) are the normal and shear stiffnesses of the discontinuity, and Δu_n and Δu_s are the increments of normal and shear relative displacement. Interaction between blocks can be formulated in terms of stresses:

$$\Delta \sigma_n = \Delta F_n / l$$

$$\Delta \sigma_s = \Delta F_s / l$$

where l is the contact length, while $\Delta \sigma_n$ and $\Delta \sigma_s$ are the normal and shear stress increments.

As a consequence, Eqs (5) and (6) can be replaced by Eqs (7) and (8):

$$\Delta \sigma_n = JK_n \Delta u_n \quad (7)$$

$$\Delta \sigma_s = JK_s \Delta u_s \quad (8)$$

with JK_n and JK_s (stress per length) as normal and shear stiffnesses of the discontinuity.

At each contact point, the increments of stress are calculated from Eqs (7) and (8) and added to the existing

stresses in order to verify the Mohr–Coulomb shear failure criterion along the discontinuity with no tension allowed along the discontinuity ($\sigma_n \geq 0$):

$$|\sigma_s| \leq c + \mu \sigma_n \quad (9)$$

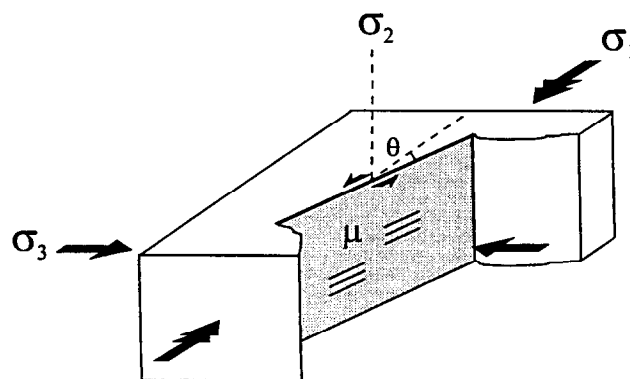
where c and μ are, respectively, the cohesion (inherent shear strength) and the coefficient of friction on the pre-existing discontinuity (that is also the tangent of the angle of friction).

Contact forces are updated and integrated in Eq. (2) for the next time step, and so on until the system converges towards a steady state. More detailed formulation of the calculation is readily available in the well-documented paper by Last and Harper (1990).

Note that information is always taken at the contact points between blocks (that is, along the discontinuities). Because the distinct-element method enables one to take into account the different rheological domains (considering different mechanical properties in each block, which means different values of d , E , ν) as well as the mechanical discontinuities (with a displacement law and a friction law) such as for pre-existing faults, it is particularly suitable for analysing the mechanical behaviour of pre-fractured geological domains. Several modelling experiments have already demonstrated the ability of this method to solve geological problems involving fault behaviour (Homberg, 1993; Sassi *et al.*, 1993; Dupin *et al.*, 1994; Auzias, 1995; Hu, 1995).

In our modelling, deformation of the medium is thus controlled by Newton's second law (Eq. 2). Deformation is continuous in the blocks and follows the elasticity theory (Eq. 4), sliding along discontinuities is allowed and controlled by a force–displacement law (system of Eqs 5 & 6, or system of Eqs 7 & 8), and shear stresses along the discontinuities are limited according to a Mohr–Coulomb friction law (Eq. 9). As a consequence, the required parameters to solve the calculation are those contained in Eqs (2), (4), (7), (8) and (9). They include (i) the density (d), the Young's modulus (E) and the Poisson's ratio (ν) of the medium, and (ii) the coefficient of friction (μ), the cohesion (c) and the normal and shear stiffnesses (JK_n and JK_s) of the discontinuities.

We carried out a systematic study by constructing models with various boundary conditions and considering different fault strikes with different coefficient of friction. Each model consists of a homogeneous isotropic elastic medium (see Eq. 4), cut by a single finite discontinuity that obeys a Mohr–Coulomb shear failure criterion (Eq. 9). The medium is submitted to stress boundary conditions (Fig. 4), such that σ_1 and σ_3 are horizontal and trend N–S and E–W, respectively ($\sigma_1 \geq \sigma_2 \geq \sigma_3$, compressive stresses being positive). For the medium, we chose average rheological properties of limestones (often present in platform domains such as in the Jura) as given in tables of rock mechanical properties (Lama and Vutukuri, 1978): the density (d) is 2700 kg m^{-3} , the Young's modulus (E) is 60 GPa and the



- ★ $0^\circ \leq \theta \leq 90^\circ$
- ★ $10 \text{ MPa} \leq (\sigma_1 - \sigma_3) \leq 100 \text{ MPa}$
- ★ $0.01 \leq \mu \leq 1$

Fig. 4. Geometry, mechanical properties and boundary conditions of the 2-D distinct-element models. The discontinuity (shaded plane) is characterized by the angle, θ , between its strike and the direction of applied σ_1 and its friction coefficient, μ . The rock mass, with mechanical properties of limestones, is submitted to boundary stress conditions, with maximum and minimum horizontal principal stresses (σ_1 and σ_3) as double and simple arrows, respectively. The ranges of the three parameters, θ , $(\sigma_1 - \sigma_3)$ and μ , are given.

Poisson's ratio ν is 0.25. Because of the stress range considered (described later), the cohesion (c) of the discontinuity equals zero (Byerlee, 1978). For normal and shear stiffnesses, we chose the values proposed by Dupin *et al.* (1994); JK_n and JK_s are, respectively, equal to 198 GPa m^{-1} and 200 GPa m^{-1} . We examined the stress distributions, changing step by step the values of the following three parameters (Fig. 4): (1) the angle, θ , between the strike of the discontinuity and the axis of the maximum horizontal principal stress, σ_1 , at the boundaries; (2) the differential stress magnitude ($\sigma_1 - \sigma_3$) of the applied stress state; and (3) the friction coefficient of the discontinuity, μ .

Stress perturbations as a function of the geometric relation between discontinuity and regional stress state

It is admitted that pre-existing planes of favourable strike relative to the applied external stresses can be reactivated (Jaeger and Cook, 1969). We therefore constructed models considering various strikes of the discontinuity, stress boundary conditions and friction on the discontinuity being constant. The strike of the discontinuity is represented by the angle θ (defined above) and ranges between 0° and 90° (Fig. 4). As an example, Fig. 5 illustrates the stress patterns calculated for $\theta = 20^\circ$ and $\theta = 60^\circ$, with μ and $(\sigma_1 - \sigma_3)$ being in both experiments respectively equal to 0.01 and 50 MPa. Whatever the value of θ , the stress distribution showed particular properties, illustrated in Fig. 5(a & b). (1) The stress deviations are present only if sliding on the discontinuity occurs. (2) The stress distribution is

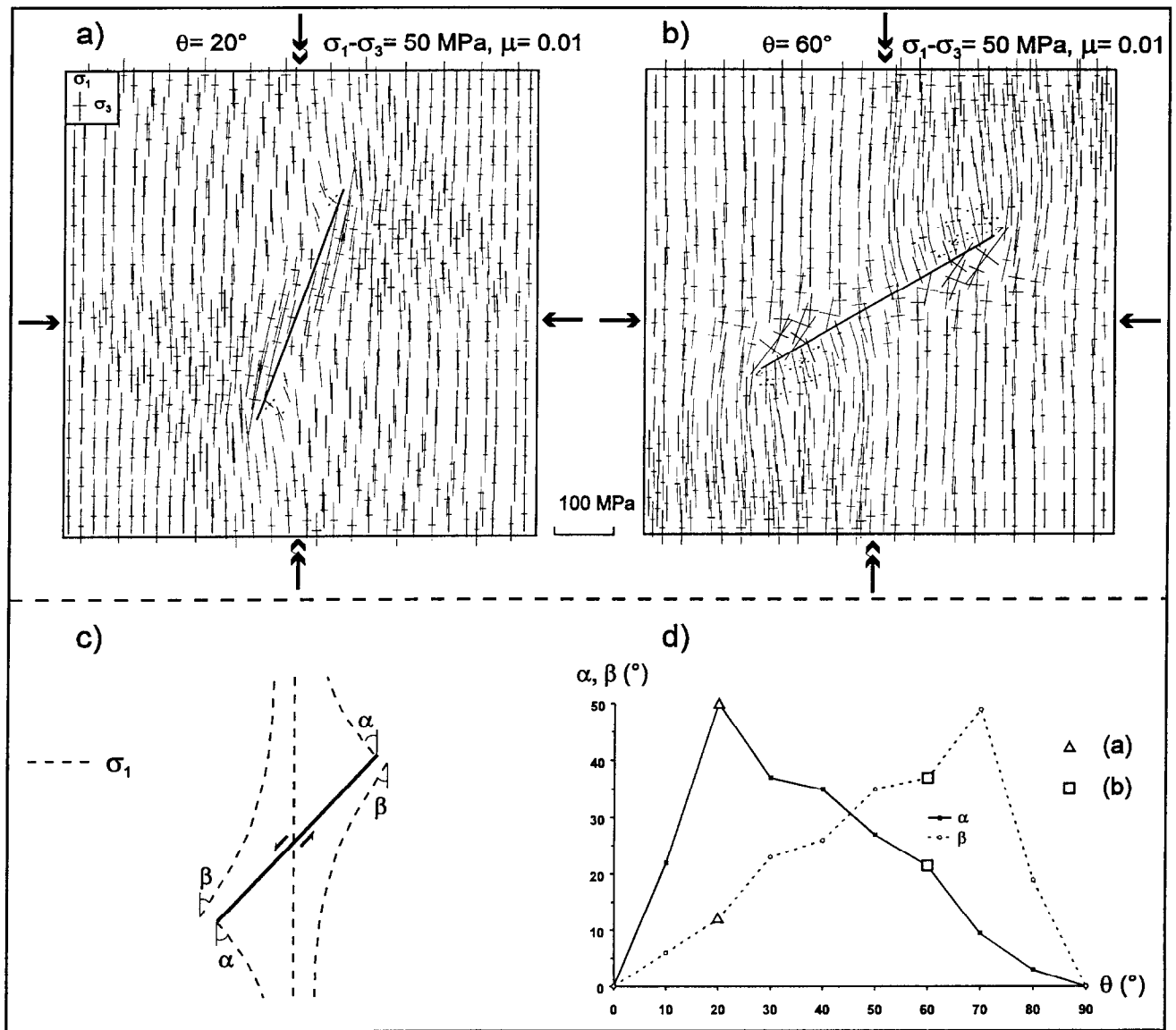


Fig. 5. 2-D distinct-element models of stress perturbations around a single discontinuity (thick line) as a function of the strike of the discontinuity (θ) relative to the applied stress. Stress distributions (σ_1 and σ_3) for (a) $\theta = 20^\circ$ and (b) $\theta = 60^\circ$. For both models, $(\sigma_1 - \sigma_3) = 50$ MPa and $\mu = 0.01$. Compressive and tensile stresses are shown as continuous and dotted lines, respectively. Magnitudes of σ_1 and σ_3 are proportional to the length of the lines (see scale). Double and simple black arrows: directions of σ_1 and σ_3 at the boundaries, respectively. θ , α , β , μ and $(\sigma_1 - \sigma_3)$ are as defined in the text. (c) σ_1 trajectories around a vertical strike-slip fault based on the Anderson (1951) model, and definition of α and β . (d) Variations of α and β as a function of θ . The values of α and β for the two models presented in (a) and (b) are labelled as open triangles and squares, respectively.

symmetrical, relative to the centre of the discontinuity. (3) The stress perturbations are observed in the close vicinity of the discontinuity and near its tips. (4) At the southwestern tip of the discontinuity, σ_1 is rotated in a clockwise sense in the western block in such a way that σ_1 tends to become parallel to the discontinuity as stress magnitudes are increasing; in the eastern block, σ_1 is rotated counterclockwise so that it tends to become perpendicular to the discontinuity as stress magnitudes are decreasing. Because the geological reconstructions of paleostress fields based on the analysis of brittle tectonic data do not usually provide access to paleostress magnitudes, we simply describe directional stress pertur-

bations, which will be used in comparison with geological situations.

The stress distributions illustrated in Fig. 5(a & b) are in good agreement with those predicted by Anderson (1951) in frictionless simple shear mode, and in Fig. 5(c) with those by Ricou (1978) for faults with friction. The calculated stress perturbations are qualitatively similar, whatever the values of the different parameters (Figs 5, 7 & 8). For the sake of simplicity, we define the two angles, α and β , in order to analyse and describe these perturbations. As Fig. 5(c) shows, the angle α represents the largest deviation of the maximum horizontal principal stress σ_1 in the counterclockwise sense, whereas β

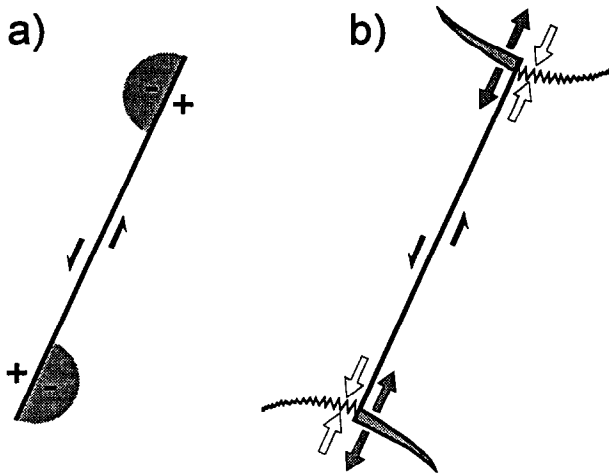


Fig. 6. Deformation near fault tips. (a) Identification of two domains in fault tips, extensional (dark grey with negative sign) and contractional (light grey with positive sign). Circular shape arbitrary. (b) Tectonic features commonly observed near fault tips at the outcrop scale (Petit and Mattauer, 1995). Extensional zones (dark grey divergent arrows) show tension gashes (dark grey) or veins. Contractional zones (light grey convergent arrows) show pressure-solution seams with stylolites.

represents its maximum deviation in the clockwise sense, in the case of a left-lateral strike-slip fault. The largest deviations of σ_1 are located in the close vicinity of fault tips in a domain which can be divided for each fault tip into two zones, contractional and extensional (Fig. 6a). This separation within the domains around the fault tips is supported by geological observation at the outcrop scale (Petit and Mattauer, 1995). Near each fault tip, the deformation is contractional on one side of the fault and extensional on the opposite side (Fig. 6b). Note these refer to relative stress values, not to absolute compression or tension. Very often, one can observe on one side of the fault stylolites which denote pressure-solution in the contractional zone (positive sign in Fig. 6a). On the opposite side, also close to the fault tip, the deformation is commonly absorbed by tension gashes and veins which denote an extensional zone (negative sign in Fig. 6a). Note that distribution of these extensional and contractional domains near fault tips is symmetrical relative to the centre of the fault (Fig. 6). The largest deviations of σ_1 are thus located in the two extensional zones of the fault tips for α , and in the two contractional ones for β (Fig. 5c). At the south tip of the fault, for example, α and β are the angles between the local trends of σ_1 axes and the direction of σ_1 applied at the boundaries of the model corresponding to the largest perturbations occurring in the eastern extensional zone and the western contractional zone, respectively (Fig. 5c, compare with Fig. 6).

Large changes occur in the amount of stress trend deviation in different models. For $\theta=20^\circ$ and $\theta=60^\circ$ (Fig. 5a & b), the two angles (α, β) are respectively equal to $(50^\circ, 12^\circ)$ and $(21.5^\circ, 37^\circ)$. For a variety of angles θ , Fig. 5(d) illustrates the variations of (α, β): α is equal to zero when $\theta=0^\circ$, increases with θ until a maximum of 50° for $\theta=20^\circ$, and then progressively decreases back to 0°

for $\theta=90^\circ$. Variations of β as a function of θ are symmetrical with those of α , relative to the value $\theta=45^\circ$. This can be easily understood; large values of α indicate that the local maximum principal stress σ_1 tends to become perpendicular to the discontinuity. In contrast, large values of β indicate that local σ_1 tends to become parallel to the discontinuity. Except for very small and very high values of θ ($\theta < 20^\circ$ and $\theta > 70^\circ$) where the plane of discontinuity is almost in the plane of one of the far-field principal stresses, α reaches high values when the angle between the discontinuity and the direction of the maximum principal stress σ_1 at the boundaries, θ , is low whereas maximum values of β are obtained for large values of θ . Thus, we conclude that major deviations are expected to occur for discontinuities for which $20^\circ < \theta < 70^\circ$ and will be located near the tips of the discontinuity. For discontinuities trending close to the axis of the maximum regional principal horizontal stress ($\theta < 45^\circ$), largest deviations (maximum angular deviations of the stress state) should occur in the two extensional zones defined by the discontinuity in such a way that σ_1 tends to become perpendicular to the discontinuities; for discontinuities trending nearly perpendicular to the axis of the maximum regional principal horizontal stress ($\theta > 45^\circ$), largest deviations will be located in the two contractional zones and should occur in such a way that σ_1 tends to become parallel to the discontinuities.

Stress perturbations as a function of the magnitude of the regional differential stress ($\sigma_1 - \sigma_3$)

Worldwide stress measurements (e.g. McGarr and Gay, 1978) indicate that, for the first few kilometres of the crust where brittle deformation plays a major role, stresses do not generally exceed 100 MPa. Here, we consider a differential stress within the range of 10 MPa to 100 MPa in order to characterize stress perturbations in the shallow brittle part of the crust in all contexts of deformation (platforms as well as collision belts). σ_3 was thus fixed at 10 MPa and we increased the magnitude of σ_1 with a step of 10 MPa from 20 MPa to 110 MPa.

Figure 7(a & b) illustrates stress deviations around a discontinuity characterized by $\theta=30^\circ$ and $\mu=0.12$. The couple (α, β) is equal to $(8^\circ, 4.5^\circ)$ and $(35^\circ, 20^\circ)$ when $(\sigma_1 - \sigma_3) = 30$ MPa and $(\sigma_1 - \sigma_3) = 90$ MPa, respectively. With $(\sigma_1 - \sigma_3)$ increasing from 10 MPa to 100 MPa α and β increase progressively until threshold values (Fig. 7c & d) which are fixed by the strike of the discontinuity relative to the applied σ_1 (Fig. 5d). Note that, if the friction coefficient on the plane increases, these maximum values of α and β are reached for a larger differential stress (Fig. 7c & d). Other models that we performed, not presented in this paper, indicate that for a constant magnitude of the differential stress, and when sliding occurs, the amount of stress perturbations decreases with increasing absolute stress magnitudes at boundaries. This can be compared with the results of rock mechanics

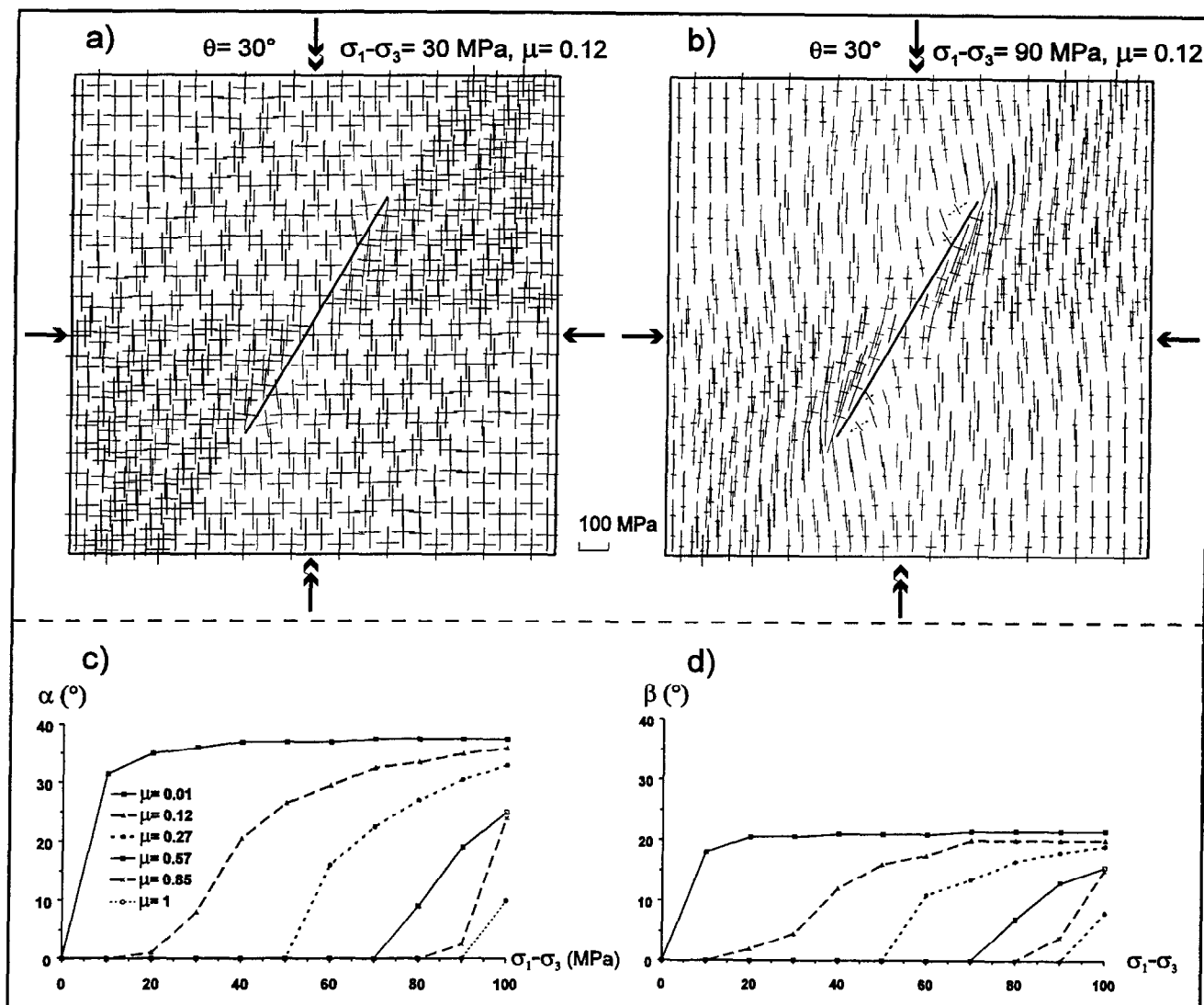


Fig. 7. 2-D distinct-element models of stress perturbations around a single discontinuity as a function of the magnitude of the differential stress ($\sigma_1 - \sigma_3$). (a) and (b) Stress distribution (σ_1 and σ_3) for ($\sigma_1 - \sigma_3$) = 30 MPa and ($\sigma_1 - \sigma_3$) = 90 MPa, respectively. For both models, $\theta = 30^\circ$ and $\mu = 0.12$. Captions as for Fig. 5(a & b). (c) and (d) Variations, respectively, of α and β as a function of ($\sigma_1 - \sigma_3$) in MPa, for various values of the coefficient of friction on the discontinuity, μ .

experiments in which, for uniaxial compression, the increasing isotropic pressure results in an increasing differential stress magnitude for failure to occur.

Stress perturbations as a function of the coefficient of friction μ on the discontinuity

The laboratory experiments of Byerlee (1978) showed that, for normal stresses smaller than 200 MPa acting on a pre-existing fracture plane, the coefficient of friction, μ , averages 0.85 and is nearly independent of rock type. Zoback and Healy (1984) proposed a similar estimate: at depths from 0.1 to 3.7 km, the coefficients of friction deduced from *in situ* stress measurements lie within the range from 0.6 to 1. In contrast, frictional sliding experiments performed on clay-rich fault gouges of the San Andreas Fault (Morrow *et al.*, 1982) provided lower coefficients of friction, ranging from 0.15 to 0.55. In order

to consider all types of faults, we adopted a large range of friction coefficients, from $\mu = 0.01$ (that is, without significant friction) to $\mu = 1$.

In our models, such as for Figs 5, 7 & 8, the increase in the friction coefficient results in a decrease of the azimuthal stress changes. For instance, with an angle $\theta = 30^\circ$ and a differential ($\sigma_1 - \sigma_3$) = 80 MPa, the couple (α, β) decreases from ($37^\circ, 21.5^\circ$) to ($27^\circ, 16.5^\circ$) as the coefficient of friction increases from 0.01 to 0.27 (Fig. 8a & b). Figure 8(c & d) illustrates the decrease in stress perturbations with increasing friction coefficients. Note that, as μ increases, the smaller the value of ($\sigma_1 - \sigma_3$), the larger the decrease of α and β .

In the bounds of our models, the largest perturbations, for a given orientation of the discontinuity relative to the far-field stress, occur for threshold values of the friction coefficient and the differential stress. As an example, when $\theta = 30^\circ$, $\mu = 0.01$ and ($\sigma_1 - \sigma_3$) = 40 MPa, these

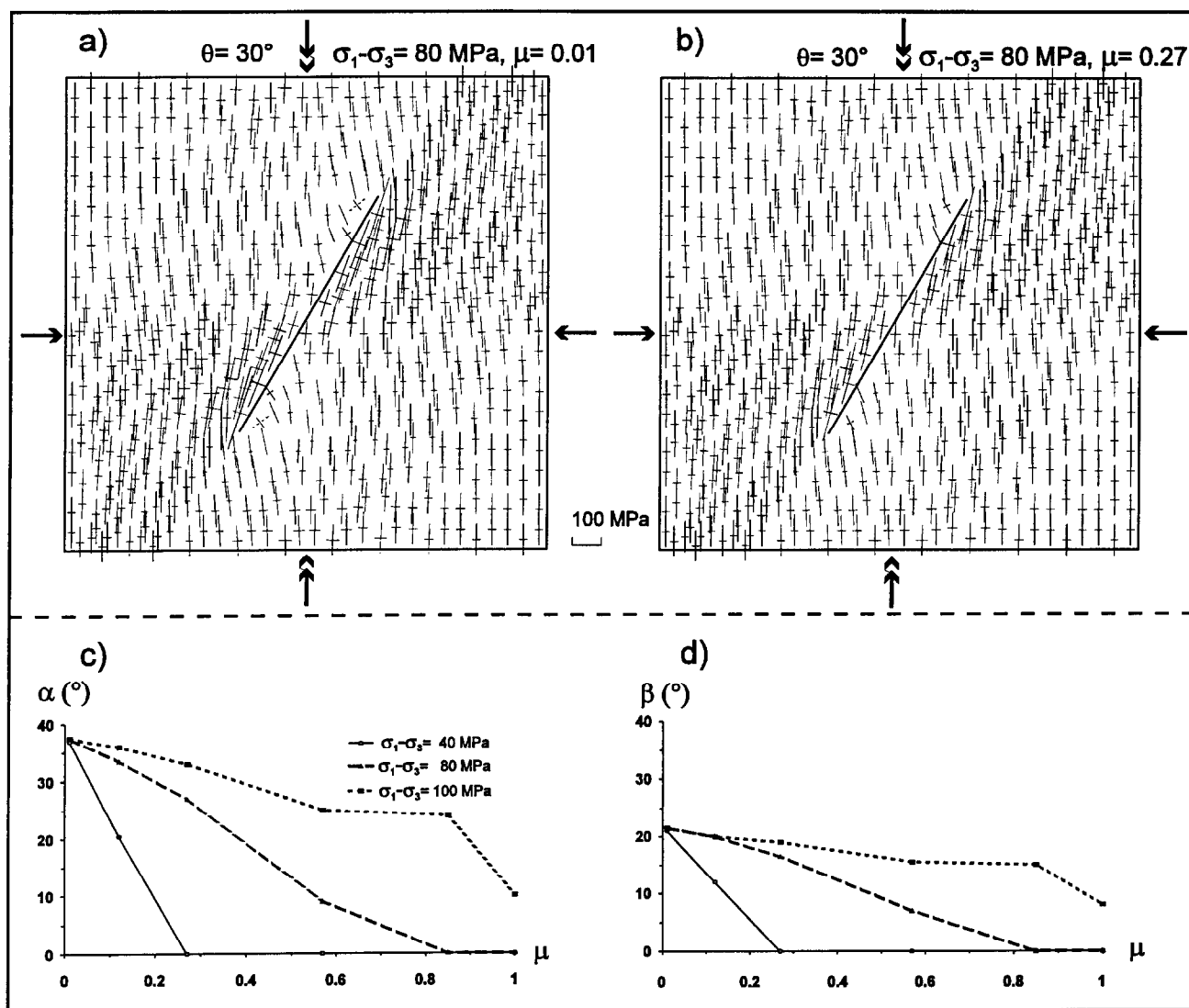


Fig. 8. 2-D distinct-element models of stress perturbations around a single discontinuity as a function of the friction coefficient, μ , on the discontinuity. (a) and (b) Stress distribution (σ_1 and σ_3) for $\mu = 0.01$ and $\mu = 0.27$, respectively. For both models, $\theta = 30^\circ$ and $(\sigma_1 - \sigma_3) = 80$ MPa. Captions as for Fig. 5(a & b). (c) and (d) Variations respectively, of α and β as a function of μ , for various values of the remote differential stress, $(\sigma_1 - \sigma_3)$.

values are reached (Figs 7c & d & 8c & d). Neither an increase in the differential stress, nor a decrease in the friction coefficient will result in an increase on the amount of stress perturbation. Below these threshold values, the amount of stress perturbations depends on both the friction coefficient on the discontinuity, μ , and the differential stress, $(\sigma_1 - \sigma_3)$, at the boundaries.

Our modelling (Figs 5, 7 & Fig. 8) confirms that the reactivation of a finite pre-existing discontinuity (that means displacement along the fault) generates changes in the local state of stresses in terms of both direction and magnitude. Stress perturbations are directly related to the existence of contractional and extensional zones at the tips of the discontinuity (Fig. 6), and are thus located predominantly near these tips. The amount of shortening and stretching in the two contractional and extensional zones is probably controlled by the amount of displacement along the discontinuity which increases for larger

values $(\sigma_1 - \sigma_3)$ and also increases for lower values of μ . As a consequence, the magnitudes of stress perturbations increase with the amount of the displacement. Figure 9 illustrates the relation of the couple (α, β) for $\mu = 0.12$ and $(\sigma_1 - \sigma_3)$ increasing from 10 MPa to 100 MPa as a function of the ratio between the displacement along the discontinuity and the discontinuity length, u/l . However, the complete characterization of the displacement as a function of both the differential stress $(\sigma_1 - \sigma_3)$ at the boundaries and the friction μ on the discontinuity, for given rock mass properties, remains difficult. This problem will be considered in a forthcoming work.

PALEOSTRESS DISTRIBUTION AROUND THE MOREZ FAULT ZONE

The structural pattern and the tectogenesis of the Jura

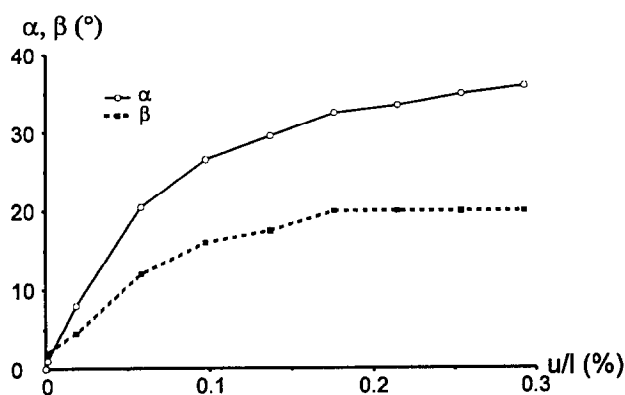


Fig. 9. Variations of α and β as a function of the ratio between the displacement along the discontinuity and the length of the discontinuity, u/l (in percentage) for $\mu=0.12$. Different data points correspond to $(\sigma_1 - \sigma_3)$ increasing from 10 MPa to 100 MPa. α , β , μ and $(\sigma_1 - \sigma_3)$ are as defined in the text.

are well known from numerous regional studies (Glan-geaud, 1949; Caire, 1960; Laubscher, 1965; Chauve and Perriaux, 1971; Chauve *et al.*, 1980). In the internal part of the belt, the Morez Fault Zone (Fig. 1) is a good example of a discontinuity reactivated as a major strike-slip fault which will provide geological constraints on our modelling (see earlier section concerning the aim of our study). The Morez Fault Zone is one of the most characteristic transverse faults of the Jura. During the Mio-Pliocene major tectonic event, folding and thrusting on both sides of the fault were accommodated independently so that the Morez Fault Zone should rather be considered as a left-lateral transfer fault. Moreover, because the Morez Fault is somewhat similar to other major radial faults of the Jura mountains (e.g. the Vuache Fault) the characterization of stress distribution around such a fault will allow improvement of our understanding of the tectogenesis of the Jura mountains.

Reconstruction of the Mio-Pliocene stress field around the Morez Fault Zone from tectonic data

The Morez Fault Zone is nearly 20 km long in the internal Jura (Fig. 1). In some places, the fault splits into two branches, about 0.25–1 km apart (Fig. 2). In order to characterize the paleostress pattern related to the activity of the Morez Fault Zone, we collected 1730 brittle tectonic data at 42 sites in natural outcrops and quarries (Fig. 10b). Striated fault planes, tension gashes and stylolites were systematically measured, as well as the attitude of bedding at each site. Inversion of the data (see below for description of the method) permits the reconstruction of three main tectonic events. In this paper, all trends (stress axes or fault strikes) are indicated in terms of azimuth (e.g. N80°W is noted as N100°). Chronology criteria (cross-cutting relations between faults, superposed striations on fault surfaces, etc.), suggest the following succession of the deformation events in this region, in agreement with that of the West

European Platform (Bergerat, 1987): (1) a N–S compression associated with the Eocene compression which occurred during the ‘Pyrenean’ orogeny; (2) a WNW–ESE extension attributed to the Oligocene continental rifting of the West European Platform; and (3) a mean NW–SE late compression corresponding to the Mio-Pliocene tectogenesis of the Jura during the Alpine orogeny. In this paper, we only describe the last event which is responsible for the main large-scale deformation.

Using the direct inversion method of Angelier (1990) we reconstructed local reduced paleostress tensors in the area of Fig. 10(b). For each site, we thus determined the orientations of the three principal stress axes, σ_1 , σ_2 , σ_3 and the ratio $\Phi = (\sigma_2 - \sigma_3)/(\sigma_1 - \sigma_3)$ (Fig. 10a). This table of data summarizes the results of paleostress inversion for the Mio-Pliocene event recognized in the area studied. The number of data used for each tensor determination ranges from 5 to 94. The quality of the results does not only increase with the number of data, but also depends on their distribution, especially where conjugate systems are present. Two misfit estimators, α' and R , support quality estimates (Fig. 10a): α' is the average observed slip-computed shear angle, within the range 0–180° as inaccuracy increases; R is a function of both the angle and the relative magnitude of shear stress, within the range of 0–200% as inaccuracy increases. Detailed presentation and discussion of these misfit estimators are given in Angelier (1990), where they are named ANG and RUP, respectively. For all calculations, we used the INVD method except for strike-slip systems of sites 10, 15, 17, 38, where stress tensors were determined with the R4DT method (see Angelier, 1991 for comparison of both methods).

Minor faults trending N145° to N155°, that is parallel to the Morez Fault, show in several cases a dextral slip older than their common sinistral slip. This earlier dextral slip, associated with sinistral slip on some minor faults trending NE–SW, is compatible with the N–S ‘Pyrenean’ compression, Eocene in age. For this reason, and also because nearly vertical faults with the same direction have been found based on seismic reflection profiling within the basement of the external Jura (Chauve *et al.*, 1988), we think that the Morez Fault already existed before the Mio-Pliocene. This indicates that during the Mio-Pliocene, the studied area was characterized by the presence of a major discontinuity in the crust, corresponding to the present Morez Fault Zone.

The data collected at five sites (sites 16, 17, 21, 28, 31) strictly located in the Morez Fault Zone, with an average spacing of about 5 km, allow accurate characterization of the displacement along this fault and the related paleostress directions. Numerous strike-slip fault data were collected on minor and major faults, and the trends of the left-lateral strike-slip faults include the direction of the Morez Fault Zone itself, which provides further evidence that the sinistral slip along this fault zone is related to the Mio-Pliocene tectonic phase. In this area,

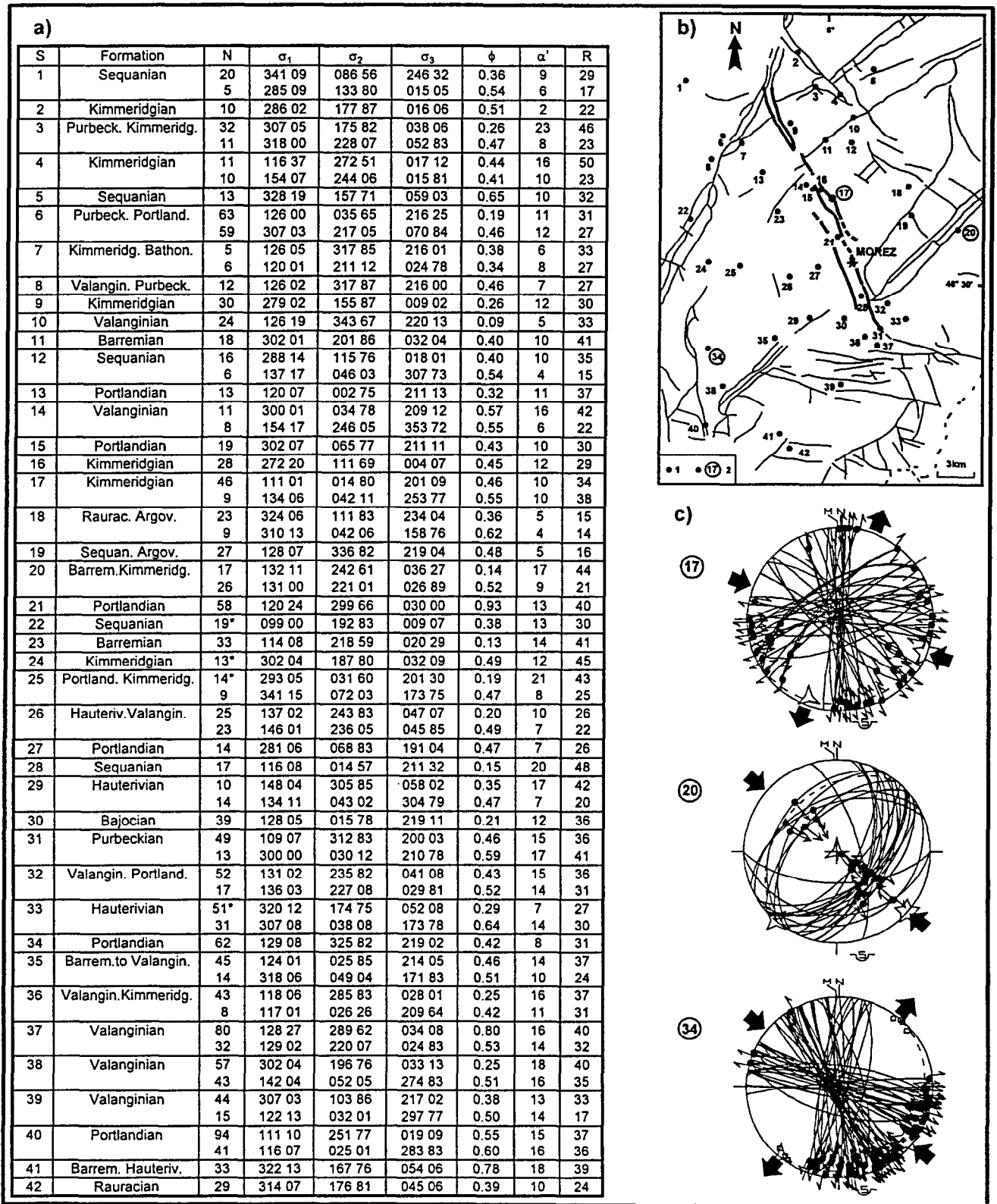


Fig. 10. Paleostress orientations related to the Mio-Pliocene compression. (a) Paleostress tensors reconstructed using fault slip data. *S*: reference number of the sites, *N*: number of fault slip data considered for calculation. σ_1 , σ_2 , σ_3 axes defined by their trends and plunges, in degrees. $\phi = (\sigma_2 - \sigma_3) / (\sigma_1 - \sigma_3)$. α' and *R*: misfit estimators (see Angelier, 1990) defined in text. *N**: back rotated stress tensor. (b) Location of sites. 1: reference of sites, 2: reference of sites mentioned in Fig. 10(c). Captions as for Fig. 2. (c) Examples of fault slip data (lower hemisphere, equal area projection). Stars with 5, 4, 3 branches (respectively): σ_1 , σ_2 , σ_3 . Convergent and divergent large black arrows: directions of σ_1 and σ_3 (respectively). Fault planes as solid great circles, slickenside lineations as dots (double and inward directed arrows for strike-slip and reverse motion, respectively). Poles to tension gashes as white squares and stylolites as black diamonds. Bedding planes as dashed great circles.

the largest amount of the Mio-Pliocene deformation was accommodated by the horizontal sinistral displacement along the Morez Fault Zone. We also studied 37 sites in the surrounding poorly deformed zones, away from other faults (Fig. 10b). This allows us to reconstruct the paleostress field in a large area around the Morez Fault Zone, but excluding most of the local perturbations related to other geological discontinuities (see section concerning the aim of our study).

In the area studied, the Mio-Pliocene compression is essentially marked by subvertical strike-slip faults. In general, the trends of minor left-lateral strike-slip faults vary between azimuths 100° and 190° , and right-lateral ones vary between azimuths 025° and 120° (Fig. 10c, sites 17 and 34). Hence, all these data cannot be accounted for by a single set of stress axes, because of the domain of azimuthal overlap (100° – 120°): a conclusion which reflects the presence of significant perturbations in the horizontal plane of the compressional trend in the area studied. In addition, reverse faults have been found in several places, striking on average N–S to $N60^\circ$ which are generally consistent, in terms of σ_1 direction, with strike-slip faults (Fig. 10a & c, site 20). Orientations of sets of stylolites and tension gashes support the computed attitudes of σ_1 and σ_3 axes.

This brittle deformation generally post-dates folding but is directly related to it. The direction of compression computed from fault slip analyses and that inferred from fold axis orientation are very similar (considering that fold axes are on average perpendicular to the maximum principal stress axis, σ_1). The σ_1 axes being nearly horizontal in all sites (Fig. 10a), we used the software proposed by Lee and Angelier (1994) in order to reconstruct paleostress trajectories through interpolation of the local directions of σ_1 . For four sites [sites 22, 24, 25, 33 with N (number of data) followed by a star] where faulting occurred before folding (Fig. 10a), we adopted the back rotated direction of σ_1 (backtilting of stress axes around the local strike of tilted strata).

We finally obtained a trajectory map of the direction of compression during the Mio-Pliocene tectonic phase around the Morez Fault Zone (Fig. 2). The direction of compression displays a very particular pattern. Away from the Morez Fault Zone, the compression trends $N130^\circ$, whereas it trends $N110^\circ$ in the very close vicinity of the fault (Figs 2 & 10a, sites 16, 17, 21, 28, 31, 36). This counterclockwise deviation of 20° is restricted to a narrow strip, 1 km wide, located along the Morez Fault Zone. In sites located less than 8 km away from the fault, the direction of compression averages $N120^\circ$, but most noteworthy is the sudden change of the direction of compression very close to the fault (compare, for example, sites 32 and 28, or sites 15 and 16 in Figs 2 & 10a). We conclude that whereas the Mio-Pliocene phase is generally characterized by a $N130^\circ$ compressional direction, such as for the neighbouring areas of the external Jura (Homberg *et al.*, 1994), it is locally deviated counterclockwise along the Morez Fault Zone. In that

way, the paleostress pattern around the Morez Fault Zone reveals stress perturbations directly related to the presence of the fault.

Modelling of the Mio-Pliocene stress field around the Morez Fault Zone

Our modelling (see above section on numerical modelling, and Figs 5, 7 & 8) shows that the presence and displacement along a discontinuity can generate local stress perturbations in terms of direction and magnitude, which vary according to several parameters. Because the Morez Fault Zone pre-existed, the observed perturbations in the direction of the Mio-Pliocene compression should be compared to those generated by the presence of a pre-existing discontinuity. The Morez Fault is a nearly vertical discontinuity and the Mio-Pliocene stress regime is mainly a strike-slip fault regime (the σ_2 axis being nearly vertical), so the study of the paleostress and displacement fields can be carried out in two dimensions and with plane strain conditions. Thus, we built a model similar to those previously described (Fig. 4) with the following conditions, as shown in Fig. 11.

- (1) The Morez Fault Zone is considered as a single $N155^\circ$ -trending discontinuity of finite length which obeys a Mohr–Coulomb friction law. For friction coefficient, we adopted the value of 0.85 proposed by Byerlee (1978).
- (2) The surrounding rock mass has been considered as an elastic medium and the following properties were used: $d = 2600 \text{ kg m}^{-3}$, $E = 55 \text{ GPa}$, $\nu = 0.29$ (see above for definitions of d , E , ν). These parameters were chosen because the surrounding rock mass essentially consists of upper Jurassic limestones (with some lower Cretaceous marls and limestones); we thus adopted the average rheological parameters determined in the Argovian limestones (Broquet *et al.*, 1993) of the Samson borehole in the Ornans plateau (external Jura), the Bajocian limestones (Mannia, personal communication, unpublished report) of a Besançon tunnel (external Jura)

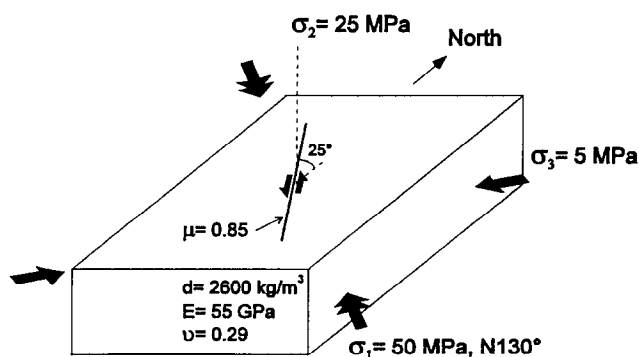


Fig. 11. Boundary conditions and mechanical properties for the 2-D distinct-element model of the Morez Fault Zone. Double and simple black arrows: direction of σ_1 and σ_3 at the boundaries, respectively. See text for significance of d , E , ν and μ .

and the upper Jurassic limestones (Riffaut, 1969) of the quarry of Hauteville (southern Jura).

(3) We applied a N130° compression at the boundaries of our model. This choice of far-field stress conditions is appropriate, because in less deformed zones such as the plateaus of the external Jura (Tschanz, 1992; Lacombe and Angelier, 1993; Homberg *et al.*, 1994), we observed little or no perturbation in the N130° trends of the Mio-Pliocene compression.

(4) σ_1 , σ_2 and σ_3 are, respectively, equal to 50 MPa, 25 MPa and 5 MPa. These values were adopted because calcite twins studies in the Burgundy platform (Lacombe and Laurent, 1992) indicate that the $(\sigma_1 - \sigma_3)$ and $(\sigma_2 - \sigma_3)$ values effectively range between 30–60 MPa and 15–25 MPa, respectively. We chose the following mean values: $(\sigma_1 - \sigma_3) = 45$ MPa, $(\sigma_2 - \sigma_3) = 20$ MPa and situated our model in the middle of the cover (depth of about 1 km). The intermediate stress, σ_2 being vertical and equal to the lithostatic load, we can thus obtain the magnitudes of σ_1 , σ_2 and σ_3 . Note that these determinations apply to dry conditions, and in terms of effective stresses should have been modified depending on water pressure and type of porosity.

As in the theoretical models (Figs 5, 7 & 8), we observe changes in the direction of compression essentially located at the tips of the fault (Fig. 12). For example, in the eastern block, at the northern tip of the fault there is a maximum clockwise rotation of the direction of compression ($\beta = 10^\circ$) where stresses increase in magnitude with a maximum of $\sigma_1 = 78$ MPa and $\sigma_3 = 11$ MPa, whereas at the southern tip, the direction of compression is deviated counterclockwise by as much as $\alpha = 21^\circ$ and stresses decrease in magnitude with a minimum of $\sigma_1 = 35$ MPa and $\sigma_3 = -4$ MPa (Fig. 12). (The significance of α and β is shown in Fig. 5c.)

These results, however, fail to explain in detail the paleostress states observed in the vicinity of the fault (Fig. 2). In the model of Fig. 12, we consider the Morez Fault as a single plane. In fact, the Morez Fault includes several segments of faults parallel to each other. Local geological observations additionally indicate that the Morez Fault consists of a large deformation zone with highly fractured rocks. The Morez Fault should thus be considered as a fault zone with a certain thickness rather than a single fault plane. Taking these parameters into account, we constructed a new model, treating the Morez Fault Zone as a discontinuity surrounded by a weak strip, 500 m wide, characterized by a small Young's modulus. Strain-stress tests on shock-damaged limestones (Hongliang and Ahrens, 1994) showed a dramatic decrease in the Young's modulus, reaching a value equal to 5% of the value for undamaged rock. From the V_p/V_s well log (V_p and V_s are the velocities of compressional and shear waves) in the Samson borehole (Broquet *et al.*, 1993), a similar variation can be calculated, although the value of the Young's modulus in the fractured rock mass reaches 70% of that of the intact rock. We therefore examine different

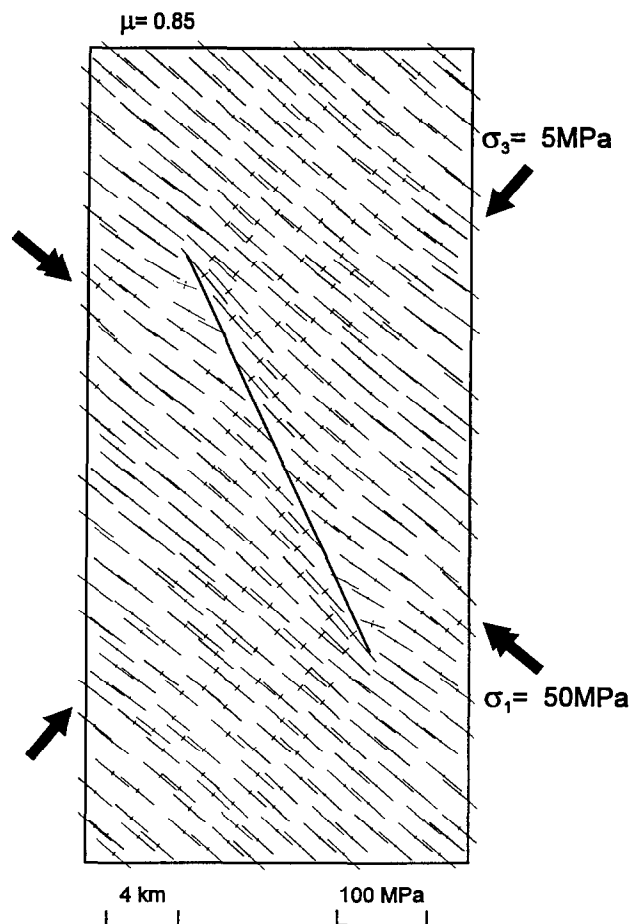


Fig. 12. 2-D distinct-element model of stress perturbations around the Morez Fault Zone considered as a single discontinuity. Double and single black arrows: direction of σ_1 and σ_3 at the boundaries, respectively. Captions as for Fig. 5(a & b).

models, with a ratio F between the Young's modulus of the weak zone and that of the surrounding medium ranging from 1/2 to 1/10.

Figure 13 illustrates the stress field obtained for F equal to 1/6. Comparing these results with those of the former model (Fig. 12), we note that: (1) the stress deviations increase near the tips of the discontinuity and for $F = 1/6$, α and β reach 36° and 11° , respectively; (2) the stress states in the weak zone are characterized by a counterclockwise rotation, which increases as F decreases. For $F = 1/6$, this rotation is 20° on average and σ_1 trends are N110°. Far away from the fault, no directional perturbation is observed, as before.

DISCUSSION

This modelling accounts well for the actual paleostress pattern determined through inversion of brittle tectonic data (Fig. 2). The direction of the Mio-Pliocene compression is regularly trending N130°, except along the Morez Fault where it trends N110°; this deviation is well accounted for by the distinct-element model (compare Figs 2 & 13). We conclude that the reactivation of the

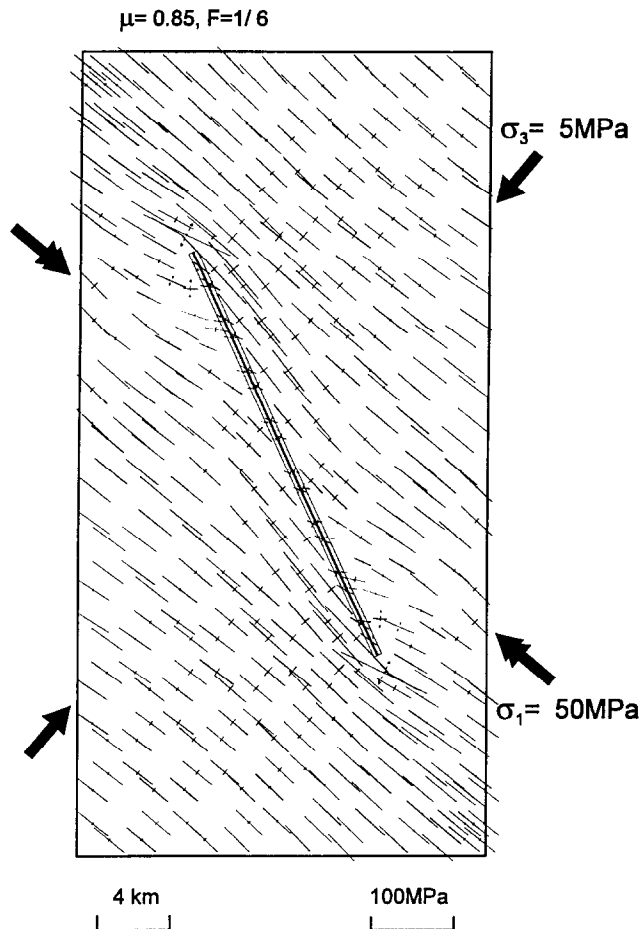


Fig. 13. 2-D distinct-element model of stress perturbations around the Morez Fault Zone considered as a single discontinuity within a weak zone. Double and single black arrows: direction of σ_1 and σ_3 at the boundaries, respectively. Shaded zone: weak strip with a smaller Young's modulus. Pre-existing discontinuity as thick line. Captions as for Fig. 5(a & b). See text for significance of F . Compare with Fig. 2.

Morez Fault Zone and the presence of a zone of weak fractured rocks related to this reactivation play a major role in the accommodation of the Mio-Pliocene deformation in the area studied. This interpretation resembles that of Zoback *et al.* (1987) concerning the San Andreas Fault; although the origin of the weakness of the fault zone is different, deviations of the present-day stress field in the vicinity of the San Andreas Fault have also been related to the weakness of the fault zone.

However, in contrast with modelling experiments, our field study did not provide evidence of significant stress changes near the tips of the fault (compare Figs 2 & 13). Two explanations can account for this apparent discrepancy.

(1) The location of the southern tip is difficult to define precisely and the fault zone may extend farther south. The absence of suitable outcrops did not allow determination of paleostress states in this southern area. Concerning its northern tip, the Morez Fault terminates against a fault zone that represents the transition towards the Champagneole Fault Zone and the Chau du Dombief Thrust which trend N18° and N33°, respectively (Fig. 2).

This major fault zone separates the external Jura from the internal one. In this area, the stress states may be simultaneously influenced by these three fault zones (Morez, Champagneole and Chau du Dombief Fault Zones).

(2) The friction on the Morez Fault Zone may be larger than that defined in the model, so that the perturbations near its tips should be smaller. Furthermore, it is likely that the friction coefficient along the fault was variable and increasing near the tips, resulting in less perturbations there. Because it is still difficult to correctly quantify the amount of displacement along the fault (the geological structure differs within the two blocks separated by the Morez Fault because strike-slip and folding developed simultaneously), we cannot check the amount of friction on this fault.

However, our modelling leads us to conclude that, for faults surrounded by a high deformation zone and in compressive deformational contexts, large stress perturbations will occur along the discontinuities in such a way that σ_1 tends to become perpendicular to the discontinuities. In other areas of the Jura, paleostress reconstructions (Homberg *et al.*, 1994 and work in progress) also indicate that the direction of the Mio-Pliocene compression is locally deviated near major pre-existing fault zones (such as for the Euthe Fault Zone), in such a way that σ_1 tends to become perpendicular to the fault trend. We conclude that the mechanical decoupling within the crust significantly influenced the accommodation of the Mio-Pliocene deformation in the Jura mountains.

CONCLUSIONS

Based on the results of 2-D distinct-element modelling and field studies (Jura mountains), it appears that, in terms of stress orientation, pre-existing structures in the crust play a major role in the accommodation of the later deformation. The reactivation of pre-existing discontinuities of various strikes is responsible for major stress perturbations, with directional deviations as large as 50°. We have shown that the magnitude of the directional deviations varies as a function of (1) the magnitude of the remote differential stress ($\sigma_1 - \sigma_3$), (2) the rheological properties of the discontinuity (including the weakness of the fractured fault zone), and (3) the strike of the pre-existing discontinuity relative to the far-field stress.

Considering a fractured crust submitted to a strike-slip tectonic regime (as for the Morez Fault case), the stress deviations (e.g. Figs 5, 7 & 8) occur in the close vicinity of reactivated discontinuities and, for the largest ones (in terms of angles of deviation), they occur as follows. First, for discontinuities trending close to the far-field direction of compression, σ_1 tends to become perpendicular to the discontinuity, but only in the extensional zones near fault tips (Fig. 6). Second, for discontinuities trending nearly perpendicular to the far-field direction

of compression, σ_1 tends to become parallel to the discontinuity, but only in the contractional zones near fault tips (Fig. 6). Third, σ_1 tends to become perpendicular to the faults where high deformation occurs and rocks are crushed and this perturbation is distributed along the fault trace (Fig. 13).

Stress deviations induced by fault reactivation are related to the decreasing amount of slip along the faults that leads to the existence of contractional and extensional zones at fault tips (Fig. 6). Stress perturbations are thus located at the tips of the faults. This point is of great importance. During one tectonic episode, the slip patch of a fault zone can differ at each seismic event. Consequently, edges of the slip patch also move. A stress state at a given place can thus vary in trend because of slip patch migration; it may successively adopt a perturbed direction (due to the proximity of the slip patch edges) during one seismic event and later adopt the orientation of the far-field stress state (due to a larger distance to the slip patch edges). This gives rise to the idea that, in compressional contexts for instance, several stress states characterized by different directions of compression at a single site close to a main fault zone can be related to a single tectonic event.

We also conclude that stress perturbations occur more probably in large deformation domains because (1) large faults may appear during the deformation and then act as major discontinuities, and (2) a high differential stress allows larger displacements along faults and induces larger directional stress deviations. In contrast, stress states reconstructed in platform areas often reflect the orientation of the far-field stress. Thus, considering the Jura mountains, the fan-shaped distribution of the direction of the Mio-Pliocene compression proposed by several authors (Plessmann, 1972; Tschanz, 1990; Philippe, 1993) may probably be explained (at least in part) by the activity on the major faults. The average Mio-Pliocene compressional trends in the Jura are N70° in its southern part, N130° in the centre, and N160° in its northeastern part; that is nearly perpendicular to the successive strikes of the major faults (N145°, N45° and N80°, respectively). In addition to the indenter effect due to the Alpine collision, and considering at a wider scale the results of our modelling, the mechanical decoupling within the crust of the Jura mountains may be partly responsible for the fan-shaped distribution of the Mio-Pliocene direction of compression, considering the orientation of the major zones of weakness.

Acknowledgements—The authors would like to thank the two reviewers, S. Katternhorn and B. Maillot, for their constructive comments on the manuscript. This work is supported by the Université Pierre et Marie Curie (U.P.M.C.) and the Institut Français du Pétrole (I.F.P.).

REFERENCES

- Anderson, E. M. (1951) *The Dynamics of Faulting*, 2nd edn. Oliver and Boyd, Edinburgh.
- Angelier, J. (1990) Inversion of field data in fault tectonics to obtain the regional stress. III: A new rapid direct inversion method by analytical means. *Geophysical Journal International* **103**, 363–376.
- Angelier, J. (1991) Inversion directe et recherche 4D: comparaison physique et mathématique de deux modes de détermination des tenseurs de paléocontraintes en tectonique de faille. *Comptes rendus de l'Académie des Sciences, Paris Serie II* **312**, 213–218.
- Arthaud, F. and Laurent, P. (1995) Contraintes, déformation et déplacement dans l'avant-pays Nord-pyrénéen du Languedoc méditerranéen. *Geodynamica Acta* **8**, 142–157.
- Auzias, V. (1995) Contribution à la caractérisation tectonique des réservoirs fracturés. Unpublished Ph.D. thesis, Université des Sciences et Techniques du Languedoc, Montpellier.
- Bergerat, F. (1987) Stress fields in the European platform at the time of Africa-Eurasia collision. *Tectonics* **6**, 99–132.
- Broquet, T. P., Mania, J. and Rampoux, N. (1993) Anisotropie acoustique et sismique des calcaires fissurés aquifères. *Bulletin de la Société géologique de France* **164**, 553–563.
- Byerlee, J. D. (1978) Friction of rocks. *Pure and Applied Geophysics* **116**, 615–626.
- Caire, A. (1960) Problèmes de tectonique et de morphologie jurassiennes. *Livre à la mémoire de P. Fallot. Mémoire hors série de la Société géologique de France II* 105–158.
- Chauve, P. and Perriaux, J. (1974) Le Jura. In *Géologie de la France*, pp. 443–464. Doin, Paris.
- Chauve, P., Enay, R., Fluck, P. and Sittler, C. (1980) Vosges, fossé rhénan, Bresse, Jura. In *Géologie des Pays Européens*, coord. C. Lorenz, pp. 357–431. Dunod, Paris.
- Chauve, P., Martin, J., Petitjean, E. and Sequeiros, F. (1988) Le chevauchement du Jura sur la Bresse: données nouvelles et réinterprétation des sondages. *Bulletin de la Société géologique de France Série IV* **8**, 5, 861–870.
- Choi, P. Y. (1996) Reconstitution des paléocontraintes en tectonique cassante: méthodes et applications en domaines continentaux déformés (Corée, Jura). Unpublished Ph.D. thesis, Université P. et M. Curie, Paris.
- Cundall, P. A. (1971) A computer model for simulating progressive, large scale movement in blocky rock systems. In *International Symposium on Rock Mechanics*. International Society of Rock Mechanics, Nancy, **II-8**.
- Cundall, P. A. (1980) UDEC, a generalised distinct element program for modelling jointed rock. *U.S. Army European Research Office and Defence Nuclear Agency, Contract Report DAJA 37-39-C-0548*.
- De Charpal, O., Trémolières, P., Jean, F. and Masse, P. (1974) Un exemple de tectonique de plate-forme: les causes majeures (Sud du massif central, France). *Revue de l'Institut français du Pétrole* **29**, 641–659.
- De Ruig, M. J. (1990) Fold trends and stress deviation in the Alicante fold belt, southeastern Spain. *Tectonophysics* **184**, 393–403.
- Dupin, J. M., Angelier, J. and Sassi, W. (1994) L'hypothèse de jeux de failles indépendamment contrôlés par un état de contrainte unique est-elle valable? Une approche numérique 3D. *Bulletin de la Société géologique, de France* **165**, 317–328.
- Gehring, A. U., Keller, P. and Heller, F. (1991) Paleomagnetism and tectonics of the Jura arcuate mountain belt in France and Switzerland. *Tectonophysics* **186**, 269–278.
- Glangeaud, L. (1949) Les caractères structuraux du Jura. *Bulletin de la Société géologique, de France Série XIX* **43**, 669–688.
- Guillaume, S. and Guillaume, A., compilers (1969) Carte géologique de la France, Morez-Bois d'Amont (published by B.R.G.M.). Scale: 1/50000. Sheet: XXXIII-XXXIV-27.
- Homberg, C. (1993) L'évolution tectonique du Jura externe au Cénozoïque: de l'analyse des déformations cassantes à la distribution des contraintes autour d'un accident pré-existant. Unpublished D.E.A. Memoir, Université Paris-Sud, Orsay.
- Homberg, C., Angelier, J., Bergerat, F. and Lacombe, O. (1994) Nouvelles données tectoniques dans le Jura externe: apport des paléocontraintes. *Comptes rendus de l'Académie des Sciences, Paris* **318**, 1371–1377.
- Hongliang, H. and Ahrens, T. J. (1994) Mechanical properties of shock-damaged rocks. *International Journal of Rock Mechanics, Mining Science and Geomechanics Abstracts* **31**, 525–533.
- Hu, J. C. (1995) Modélisation numérique et analyse tectonique régionale: le cas de Taiwan. Unpublished Ph.D. thesis, Université P. et M. Curie, Paris.
- Jaeger, J. C. and Cook, N. G. (1969) *Fundamentals of Rock Mechanics*, 3rd edn. Chapman & Hall, London.
- Lacombe, O. and Laurent, P. (1992) Détermination of principal stress

- magnitudes using calcite twins and rock mechanics data. *Tectonophysics* **202**, 83–93.
- Lacombe, O. and Angelier, J. (1993) Evolution tectonique du Jura externe au Cénozoïque et perturbations de contraintes dans la zone transformante Rhin-Saône. *Comptes rendus de l'Académie des Sciences, Paris* **317**, 1113–1120.
- Lacombe, O., Angelier, J., Byrne, D. and Dupin, J. M. (1993) Eocene-Oligocene tectonics and kinematics of the Rhine-Saône continental transform zone (eastern France). *Tectonics* **12**, 874–888.
- Lama, R. D. and Vutukuri, V. S. (1978) *Handbook on Mechanical Properties of Rocks*, Vol. II, Appendix II. Trans Tech Publications.
- Last, N. C. and Harper, T. R. (1990) Response of fractured rock subject to fluid injection Part I: Development of a numerical model. *Tectonophysics* **172**, 1–31.
- Laubscher, H. P. (1965) Ein kinematisches Modell der Juraufaltung. *Eclogae Geologicae Helveticae* **58**, 231–318.
- Lee, J. C. and Angelier, A. (1994) Paleostress trajectories maps based on the results of local determinations: the "lissage" program. *Computers and Geosciences* **20**, 161–191.
- Mc Garr, A. and Gay, N. C. (1978) State of stress in the Earth's crust. *Annual Review of Earth and Planetary Science* **6**, 405–436.
- Mattauer, M. and Mercier, J. (1980) Microtectonique et grande tectonique. *Mémoire hors série de la Société géologique de France* **10**, 141–161.
- Morrow, C. A., Shil, L. Q. and Byerlee, J. D. (1982) Strain hardening and strength of clay-rich fault gouges. *Journal of Geophysical Research* **87**, 6771–6780.
- Osokina, D. N. (1988) Hierarchical properties of a stress field and its relation to fault displacements. *Journal of Geodynamics* **10**, 331–344.
- Paris, P. C. and Sih, G. C. (1965) Stress analysis of cracks. In *Symposium on Fracture Toughness Testing and Applications*, pp. 30–81. Special Technical Publication 381, American Society for Testing and Materials, Philadelphia, Pennsylvania.
- Petit, J. P. and Mattauer, M. (1995) Paleostress superimposition deduced from mesoscale structures in limestones: the Matelles exposures, Languedoc, France. *Journal of Structural Geology* **17**, 245–256.
- Phan Trong, T. (1989) Superposition et perturbation du champ des contraintes. Détermination du tenseur des contraintes et modélisation numérique. Unpublished Ph.D. thesis, Institut de Physique du Globe de Paris, Université P. et M. Curie, Paris.
- Philippe, Y. (1993) Transfer zone in the southern thrust belt (eastern France): geometry, development and comparison with analogue modelling experiments. In *Exploration and Petroleum Geology of France*, ed. A. Mascle. *E.A.P.G. Mem.* **4**.
- Plessmann, W. (1972) Horizontal stylolithen im französisch-schweizerischen Tafel und Faltenjura und ihre einpassung in den regionalen rahmen. *Geologische Rundschau* **61**, 332–347.
- Quiblier, J. A., Trémoières, P. and Zinsziner, B. (1980) A tentative fault propagation description by three-dimensional finite-element analysis. *Tectonophysics* **6**, 199–212.
- Rawnsley, K. D., Rives, T. and Petit, J. P. (1992) Joint development in perturbed stress fields near faults. *Journal of Structural Geology* **14**, 939–951.
- Rebaï, S., Philip, H. and Taboada, A. (1992) Modern tectonic stress field in the Mediterranean region: evidence for variation in stress directions at different scales. *Geophysical Journal International* **110**, 106–140.
- Ricou, L. E. (1978) Accidents régulateurs de contrainte et réorientation de contrainte. *Comptes rendus de l'Académie des Sciences, Paris* **288** **D**, 1657–1660.
- Riffaut, R. (1969) Catalogue des caractéristiques géologiques et mécaniques de quelques roches françaises. Rapport interne du Laboratoire des Ponts et Chaussées, DGRSR.
- Rispoli, R. (1981) Stress fields about strike-slip faults inferred from stylolites and tension gashes. *Tectonophysics* **75**, 29–36.
- Sassi, W., Colletta, B., Balé, P. and Paquereau, T. (1993) Modelling of structural complexity in sedimentary basins: the role of pre-existing faults in thrust tectonics. *Tectonophysics* **226**, 97–112.
- Segall, P. and Pollard, D. D. (1980) Mechanics of discontinuous faults. *Journal of Geophysical Research* **85**, 4337–4350.
- Segall, P. and Pollard, D. D. (1987) Theoretical displacements and stresses near fractures in rock: with applications to faults, joints, veins, dikes, and solution surfaces. In *Fracture Mechanics of Rock*, ed. B. K. Atkinson, pp. 277–349. Academic Press, New York.
- Trémoières, P. (1981) Mécanismes de la déformation en zones de plate-forme. Méthode et application au bassin de Paris. *Revue de l'Institut français du Pétrole* **36**, 395–428.
- Tschanz, X. (1990) Analyse de la déformation du Jura central entre Neuchâtel (Suisse) et Besançon. *Eclogae Geologicae Helveticae* **83**, 543–558.
- Tschanz, X. (1992) Analyses structurales et microstructurales dans le Jura central franco-suisse. Essai d'interprétation cinématique. Unpublished Ph.D. thesis, Université de Neuchâtel.
- Villemin, T. (1986) Tectoniques en extension, subsidence et fracturation: le fossé rhénan et le bassin sarro-lorrain. Unpublished Ph.D. thesis, Université P. et M. Curie, Paris.
- Xiahoan, L. (1983) Perturbations de contraintes liées aux structures cassantes dans les calcaires fins du Languedoc. Observations et simulations mathématiques. Unpublished Ph.D. thesis, Université des Sciences et Techniques du Languedoc, Montpellier.
- Zoback, M. D. and Healy, J. H. (1984) Friction, faulting, and "in situ" stress. *Annales Geophysicae* **2**, 689–698.
- Zoback, M. D., Zoback, M. L., Mount, V. S., Suppe, J., Eaton, J. P., Healy, J. H., Oppenheimer, D., Reasenber, P., Jones, L., Raileigh, C. B., Wong, I. G., Scotti, O. and Wentworth, C. (1987) New evidence on the state of stress of San Andreas fault system. *Science* **238**, 1105–1111.